AIP Journal of Applied Physics

Origins of dielectric response and conductivity in (Bi1−x Nd x)FeO3 multiferroic ceramics

C.-S. Tu, W.-C. Yang, V. H. Schmidt, and R. R. Chien

Citation: Journal of Applied Physics **110**, 114114 (2011); doi: 10.1063/1.3667204
View online: http://dx.doi.org/10.1063/1.3667204
View Table of Contents: http://scitation.aip.org/content/aip/journal/jap/110/11?ver=pdfcov
Published by the AIP Publishing

Origins of dielectric response and conductivity in $(Bi_{1-x}Nd_x)FeO_3$ multiferroic ceramics

C.-S. Tu,[1,2,a)] W.-C. Yang,[2] V. H. Schmidt,[3] and R. R. Chien[3]
[1]*Graduate Institute of Applied Science and Engineering, Fu Jen Catholic University, Taipei 242, Taiwan*
[2]*Department of Physics, Fu Jen Catholic University, Taipei 242, Taiwan*
[3]*Department of Physics, Montana State University, Bozeman, Montana 57917, USA*

(Received 3 September 2011; accepted 5 November 2011; published online 8 December 2011)

The dielectric response and conductivity have been measured in $(Bi_{1-x}Nd_x)FeO_3$ ($x = 0.0$ and 0.05) ceramics as functions of temperature and frequency. A one-dimensional across-barrier model with intrinsic barriers, B (in temperature units), every lattice constant, a, and extrinsic barriers, $B + \Delta$, every distance, d, is introduced to describe the dielectric response and conductivity. The across-barrier hopping is responsible for the high-temperature conductivity and step-like dielectric relaxation in the region of 500–800 K. Good qualitative fits of dielectric dispersion and conductivity are obtained with $d = 20$–30 nm, B = 8400–8700 K (~0.72–0.75 eV), and $\Delta = 2500$ K (~0.215 eV). The resistivity plot of scaled ρ'' versus ρ' indicates a contribution of grain boundaries or internal defects to the conductivity. © *2011 American Institute of Physics*. [doi:10.1063/1.3667204]

I. INTRODUCTION

Multiferroic materials enable a coupling interaction between ferromagnetic (FM) and ferroelectric (FE) parameters. This magnetoelectric coupling can be utilized to develop additional functionalities that induce magnetization using an external electric field or FE polarization using an external magnetic field. $BiFeO_3$ (BFO) has a high antiferromagnetic (AFM)-paramagnetic (PM) Néel temperature at $T_N = 352$–397 °C and an FE Curie temperature at $T_C = 810$–870 °C.[1,2] An *R*3c rhombohedral structure ($a_R = 5.616$ Å and $\alpha_R = 59.35°$) was reported for bulk BFO,[3] and can also be indexed based on the pseudo-cubic lattice ($a_p = 3.96$ Å).[4] The neutron diffraction of BFO suggested an FE rhombohedral-paraelectric (PE) orthorhombic transition at $T_C \cong 820$ °C.[5,6]

It has been a challenge to synthesize single-phase BFO ceramics with substantial electric polarization due to current leakage.[7,8] To enhance the FM and FE features, many studies have focused on BFO ceramics with substituted ions in the A and/or B sites of the perovskite structure.[9–11] A-site substitutions of rare-earth cations are expected to suppress the spiral magnetic modulation and enhance a, FM response.[6]

$NdFeO_3$ is known to be an orthorhombic structure with a G-type AFM Néel temperature at $T_N \cong 487$ °C.[12] From the x-ray diffraction (XRD), orthorhombic and triclinic structures were proposed in $Bi_{1-x}Nd_xFeO_3$ ceramics for $x = 0.4$–1.0 and $x = 0.2$, respectively.[12] Triclinic and pseudo-tetragonal structures were proposed in $Bi_{1-x}Nd_xFeO_3$ for $x = 0.05$–0.15 and $x = 0.175$–0.20, respectively.[13] An XRD result revealed a first-order antiferroelectric orthorhombic (*Pnam*)-PE orthorhombic (*Pbnm*) transition in $Bi_{1-x}Nd_xFeO_3$ ceramics for $0.10 \leq x \leq 0.25$.[6]

II. EXPERIMENTAL PROCEDURES

The $BiFeO_3$ (BFO) and $(Bi_{0.95}Nd_{0.05})FeO_3$ (BFO-5%Nd) ceramics were prepared by the solid state reaction method. For the synthesis of BFO, Bi_2O_3 and Fe_2O_3 powders (purity ≥ 99.0%) were weighed in a 1:1 molar ratio and then mixed in an agate mortar for more than 24 h using alcohol as a medium. The mixture was dried before calcining at 800 °C for 3 h. The calcined powder was mixed with polyvinyl acetate as a binder for granulation, and was then pressed into a disk before sintering at 750 °C for 1 h. For BFO-5%Nd ceramic, Bi_2O_3, Nd_2O_3, and Fe_2O_3 powders were weighed in a 0.95:0.05:1 molar ratio. The sintered temperature and dwelling time are 860 °C and 2 h. The real (ε') and imaginary (ε'') parts of the dielectric permittivity were obtained by using a Wayne-Kerr Analyzer PMA3260 A upon heating.

III. RESULTS AND DISCUSSION

Figure 1 shows room-temperature XRD and SEM spectra of the BFO and BFO-5%Nd ceramics. The BFO and BFO-5%Nd show a similar XRD spectrum and have a rhombohedral structure. Very minor second phases occur in BFO and BFO-5%Nd, and are possible $Bi_{25}FeO_{39}$ or $Bi_2Fe_4O_9$, as indicated by an asterisk.[3] The BFO-5%Nd exhibits less second phase, suggesting that the Nd-substitution can stabilize the single-phase perovskite structure. The grain sizes of the BFO and BFO-5%Nd ceramics vary as 0.5–2.0 and 1.0–4.0 μm, respectively, as shown in Fig. 1.

Figures 2 and 3 display dielectric permittivities, conductivities, and model fits. The results indicate two separate phenomena for both ceramics. A phase-shifted conductivity is evident at higher temperatures (>700 K), where the $\varepsilon'/\varepsilon''$ ratio is about 0.01–0.1 and corresponds to a conductivity phase shift of only a few degrees. A step-like dielectric dispersion in ε' appears in the region of 500–800 K for $f = 10$ kHz-1 MHz and is more pronounced in the BFO-5%Nd. The nearly Arrhenius behavior at higher temperatures, plotted as log σ'

a)Author to whom correspondence should be addressed. Electronic mail: 039611@mail.fju.edu.tw.

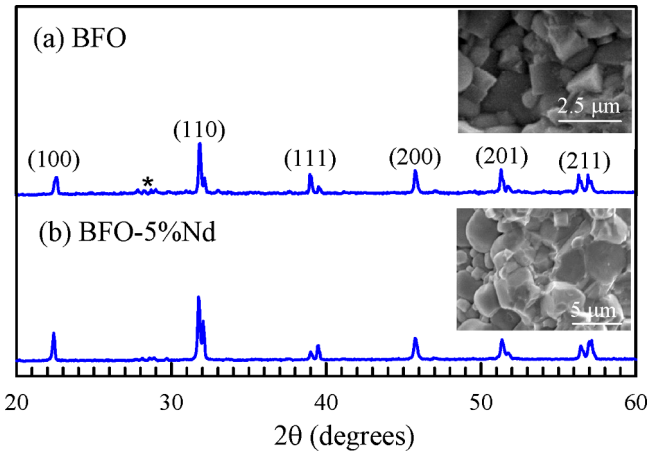

FIG. 1. (Color online) XRD and SEM of (a) BFO, and (b) BFO-5%Nd ceramics at room temperature.

versus $10^3/T$ using the relation, $\sigma' = \varepsilon'' \varepsilon_o \omega$ in Figs. 2(b) and 3(b), is the major effect of the conductivity mechanism.

To understand the conductivity and dielectric response in terms of temperature and frequency, a one-dimensional barrier model was derived, as illustrated in Fig. 4, in which B represents the intrinsic barriers spaced a distance, a, apart, where a is on the order of a lattice constant. Here, $B + \Delta$ are extrinsic barriers spaced a distance, d, apart. The attempt frequency for crossing the barriers is estimated by using $\nu = k\Theta/h$, where k, Θ, and h are the Boltzmann constant, Debye temperature, and Planck's constant. We chose

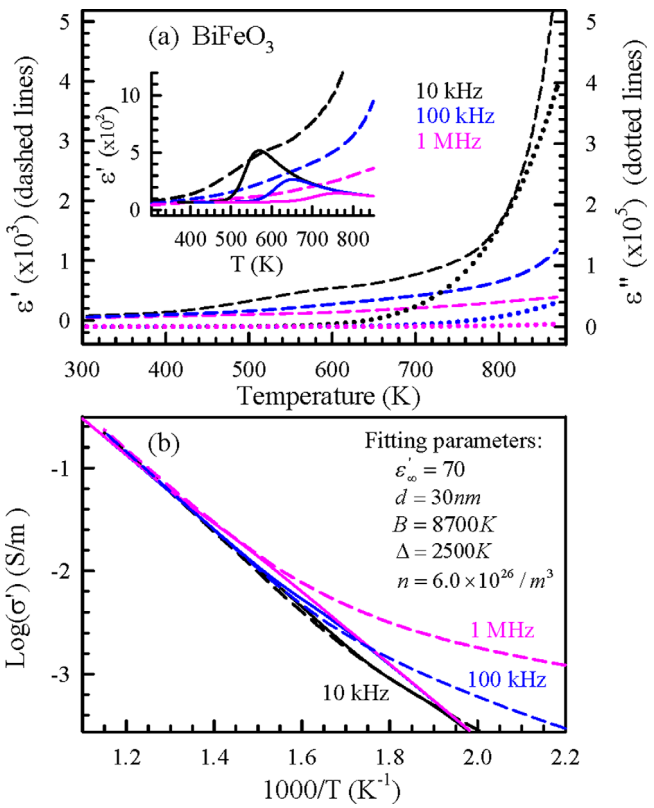

FIG. 2. (Color online) (a) ε' (dashed lines) and ε'' (dotted lines), and (b) conductivity, σ' (dashed lines), of BFO. The solid lines are fits for σ' and ε' with the parameters in (b).

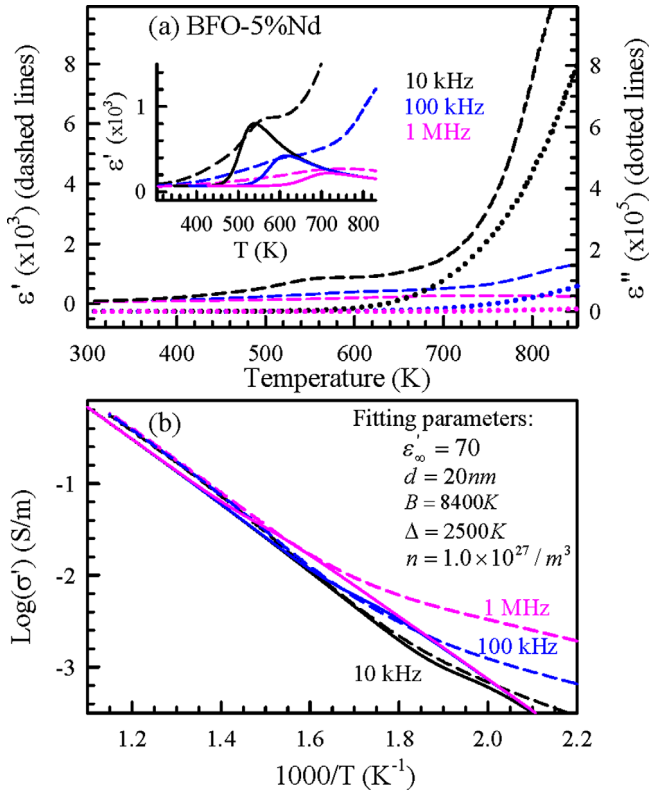

FIG. 3. (Color online) (a) ε' (dashed lines) and ε'' (dotted lines), and (b) conductivity, σ' (dashed lines) of BFO-5%Nd. The solid lines are fits for σ' and ε' with the parameters in (b).

$\Theta = 300$ K, i.e., $\nu = 6.25 \times 10^{12}$ Hz. The complex ac conductivity, $\sigma(\omega, T)$, can be defined as,

$$\sigma(\omega, T) = (J + \partial D/\partial t)/\langle E \rangle \equiv J_t/\langle E \rangle, \tag{1}$$

where J and $\partial D/\partial t$ are the position-dependent conduction current density and displacement current density, however, the total current density, J_t, is position-independent; $\langle E \rangle$ is the spatially averaged measured field. We assume conductivity with a temperature-independent carrier density, n, and carrier charge, $q = 2e$, for oxygen vacancy carriers, or $\pm e$ for hole or electron hopping conductivity carriers. The $\sigma_\infty = J/E$, taking into account that the number of carriers per unit area in a unit-cell layer on either side of a barrier layer is na, and their attempt frequency for crossing the barrier is ν, can be expressed by,

$$\begin{aligned} \sigma_\infty &= q\nu na[e^{(-kB+\frac{1}{2}qEa)/kT} - e^{(-kB-\frac{1}{2}qEa)/kT}]/E \\ &\cong (nq^2a^2\Theta/hT)e^{-B/T}. \end{aligned} \tag{2}$$

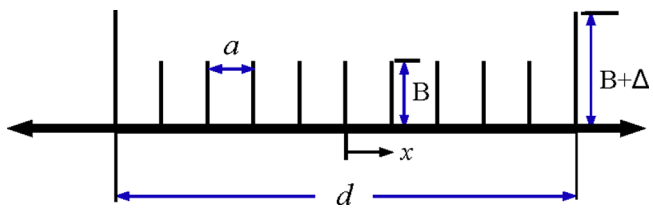

FIG. 4. (Color online) One-dimensional barrier model with intrinsic barriers, B, at spacing, a, and extrinsic barriers, $B + \Delta$, at spacing, d.

Using Gauss's law, $\partial D/\partial x = \rho$, and the diffusion equation, $\partial\rho/\partial t = \bar{D}\nabla^2\rho$, Eq. (1) becomes,

$$J = \sigma_\infty E - \overline{D}\partial\rho/\partial x = \sigma_\infty E - \sigma_\infty\tau(\partial\rho/\partial x), \quad (3)$$

where $\overline{D}$ and ρ are the diffusion coefficient and charge density. The Einstein relation, $q\overline{D} = \mu kT = (v_d/E)kT$, $\tau = kT/(nq^2)$, and $\sigma_\infty = nq\mu = nq(v_d/E)$ were used in Eq. (3). Here, v_d is the drift velocity. Taking the x derivative of Eq. (3), we have,

$$\partial E/\partial x = (\partial J/\partial x)/\sigma_\infty + \tau(\partial^2\rho/\partial x^2). \quad (4)$$

To eliminate J and E, the one-dimensional Gauss's law, $\partial E/\partial x = \rho/\varepsilon_\infty$, and continuity equation, $\partial J/\partial x = -\partial\rho/\partial t$, were used in Eq. (4), then

$$\partial^2\rho/\partial x^2 - \rho/(\tau\varepsilon_\infty) - (\partial\rho/\partial t)/(\tau\sigma_\infty) = 0. \quad (5)$$

This equation is separable and we may assume that $\rho(x,t) = f(x)e^{i\omega t}$. Then, Eq. (5) becomes

$$(\partial^2 f/\partial x^2) - \alpha^2 f = 0 \text{ and } \alpha^2 = 1/(\tau\varepsilon_\infty) + i\omega/(\tau\sigma_\infty). \quad (6)$$

The solution is $f(x) = Ae^{\alpha x} + Be^{-\alpha x}$. For a neutral material, $\rho(x=0) = 0$ at the midpoint between higher barriers is expected, i.e., $B = -A$. Then, $\rho(x,t)$ becomes $\rho(x,t) = A'\sinh(\alpha x)e^{i\omega t}$. From here on, the time dependence, $e^{i\omega t}$, will be omitted in expressions for ρ, J, and E. From Eq. (3), the current density, J, at $x = d/2$ can be expressed by,

$$J(d/2) = \sigma_\infty[E(d/2) - \tau(\partial\rho/\partial x)]e^{-\Delta/T}. \quad (7)$$

The difference in carrier density across the higher barriers is,

$$\rho(d/2) - \rho(-d/2) = 2\rho(d/2), \quad \partial\rho/\partial x \cong 2\rho(d/2)/a. \quad (8)$$

Thus,

$$J(\pm d/2) = \sigma_\infty\{E(\pm d/2) - \tau[\rho(-d/2) - \rho(d/2)]/a\}e^{-\Delta/T} = \sigma_\infty e^{-\Delta/T}\{E(\pm d/2) + 2\tau a^{-1}A'\sinh(b)\}, \quad (9)$$

where $b = \alpha d/2$. Using Eq. (3) and $\partial\rho/\partial x = A'\alpha\cosh(\alpha x)$, we obtain,

$$E(\pm d/2) = \tau A'[2a^{-1}e^{-\Delta/T}\sinh(b) + \alpha\cosh(b)](1 - e^{-\Delta/T})^{-1}. \quad (10)$$

Then, Eq. (9) becomes,

$$J(\pm d/2) = \sigma_\infty\tau A'e^{-\Delta/T}[\alpha\cosh(b) + 2a^{-1}\sinh(b)] \times (1 - e^{-\Delta/T})^{-1}. \quad (11)$$

From Eqs. (10) and (11), we can determine the total current,

$$J_t = \tau A'e^{-\Delta/T}\{\sigma_\infty[\alpha\cosh(b) + 2a^{-1}\sinh(b)] + i\omega\varepsilon_\infty[2a^{-1}\sinh(b) + e^{\Delta/T}\alpha\cosh(b)]\}(1 - e^{-\Delta/T})^{-1}. \quad (12)$$

The electric field, E, in the interval, $-d/2 < x < d/2$, can be obtained by,

$$E(x) = \int\rho(x)dx/\varepsilon_\infty = E(-d/2) + (A'/\varepsilon_\infty)\int_{-d/2}^{x}\sinh(\alpha x)dx. \quad (13)$$

Then, the average field $\langle E\rangle$ can be calculated by $\langle E\rangle = 1/d\int_{-d/2}^{d/2}E(x)dx$.

By using Eqs. (1), (12), and (13) and carrying out considerable calculations, we obtain,

$$\sigma(\omega,T) = \{\sigma_\infty e^{-\Delta/T}[2a^{-1}\sinh(b) + \alpha\cosh(b)] + i\omega\varepsilon_\infty[2a^{-1}e^{-\Delta/T}\sinh(b) + \alpha\cosh(b)]\} \times \{2a^{-1}e^{-\Delta/T}\sinh(b) + \alpha\cosh(b) + (2/d\tau\varepsilon_\infty\alpha^2)[\sinh(b) - b\cosh(b)](1 - e^{-\Delta/T})\}^{-1}, \quad (14)$$

where α and b are complex. The permittivity, $\varepsilon = \varepsilon' - i\varepsilon''$, relates to the conductivity, $\sigma = \sigma' + i\sigma''$, by $\varepsilon' = \sigma''/\varepsilon_o\omega$ and $\varepsilon'' = \sigma'/\varepsilon_o\omega$.

As shown in Figs. 2(b) and 3(b), the low-frequency conductivities, σ', of BFO and BFO-5%Nd were fitted fairly well by using Eq. (14), from which the parameters of ε'_∞, n, d, B, and Δ were obtained. The lattice constant of $a = 0.398$ nm was calculated from XRD (Fig. 1). The extrinsic-barrier distances of $d = 30$ and 20 nm for BFO and BFO-5%Nd are smaller than the grain size, implying possible internal boundaries inside the grains or defects. The $n = 6.0\times10^{26}/\text{m}^3$ for the BFO is smaller than $n = 1.0\times10^{27}/\text{m}^3$ for the BFO-5%Nd.

The solid curves in the insets of Figs. 2(a) and 3(a) are fits of ε' for $f = 10$ kHz-1 MHz by using Eq. (14) with the same parameters as given in Figs. 2(b) and 3(b). The barrier model predicts peaks whose locations fit very well with the shoulders observed in the region of 500–800 K. The measured peaks are actually shoulders because they are superimposed on upward slopes that probably result from electrode effects not considered in our model. These peaks are considerably broadened relative to the model predictions, probably due to actually having distributions of spacings, d, and barrier heights (B and Δ).

The conductivity begins to depart from the barrier-model fit near 650 K for $f = 1$ MHz. Some of this deviation could be caused by magnetoelectric coupling. The synchrotron XRD of the BFO revealed a broad minimum in the rhombohedral angle, α_R, near 650 K, due to the changes in the positions of the ions, implying a magnetoelectric coupling effect,[14] or at least a structural change that affects both the magnetic and dielectric behavior. The magnetoelectric effect in BFO measured at 9 T by Kamba *et al.*[15] was quite small, leveling out at a 0.3% increase in ε' at 300 K (the highest T reported) after peaking at 1.2% in the 225–250 K range. They attributed it to a combination of magnetoresistance and the Maxwell-Wagner effect, and termed it an improper magnetodielectric effect.

To analyze the experimental results, it is helpful to plot them in several different ways. In Figs. 2 and 3, and are plotted versus T and $10^3/T$ for various frequencies f, respectively.

for BFO and BFO-5%Nd, respectively. These plots are useful for displaying the fit of the barrier model to the data, but not for comparing the resistivity, ρ'', with ρ' at given (T,f) combinations. The correlation between the resistivity, $\rho = \rho' - i\rho''$, and the permittivity, $\varepsilon = \varepsilon' - i\varepsilon''$ is,

$$\rho = \rho' - i\rho'' = 1/\sigma = (\sigma' - i\sigma'')/(\sigma'^2 + \sigma''^2) \quad \text{and}$$
$$\sigma = i\omega\varepsilon_o\varepsilon = \omega\varepsilon_o(\varepsilon'' + i\varepsilon'). \tag{15}$$

For comparing ρ'' with ρ', we display Fig. 5 which shows log ρ'' versus log ρ' for various T, with f points indicated on each curve. The log-log plot is necessary to clearly display all ρ data because they range over several orders of magnitude.

To make the ρ'' versus ρ' plots legible on a linear plot, the resistivity was scaled for various temperatures by multiplying by an exponential factor, using the conductivity activation energies, E_a, as shown in Fig. 6. This scaling achieves an almost perfect fit to a flattened arc at higher f, where the data for different temperatures overlap well to show the entire arc. The impedance represented by the arc is much lower for BFO-5%Nd than for BFO. For lower f, the data overlap on straight lines with a small positive slope at and above 600 K, with steeper slopes for lower T. In circuit terms, this pattern can be achieved by a parallel combination of a resistor, R, and a constant phase element (CPE), in series with another CPE. Physically, the R-CPE parallel combination is usually attributed to ceramic grain boundaries or to defects, and the series CPE to electrode impedance. The

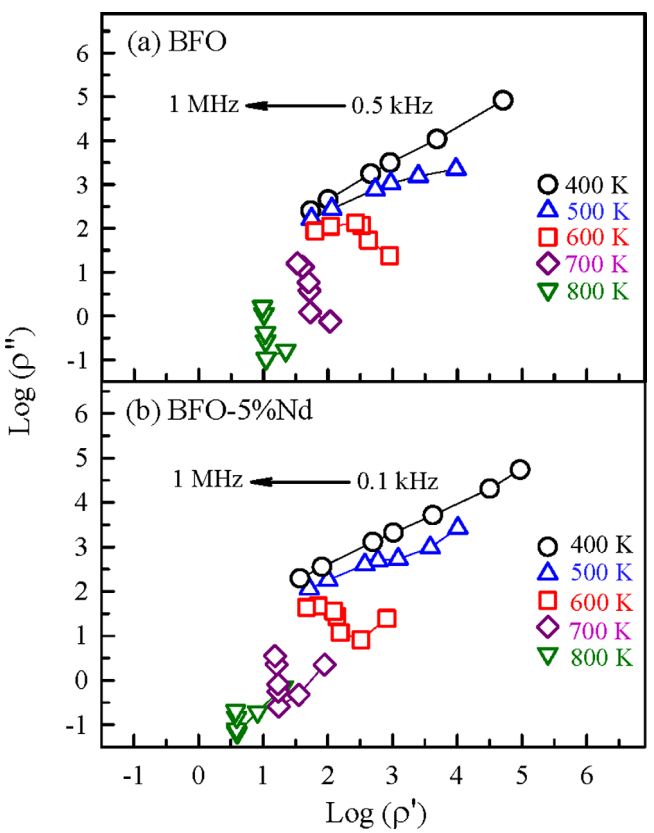

FIG. 5. (Color online) ρ'' vs ρ' in log scale at several temperatures. Frequencies are 0.1, 0.5, 10, 50, 100, 500, and 1000 kHz (from right to left).

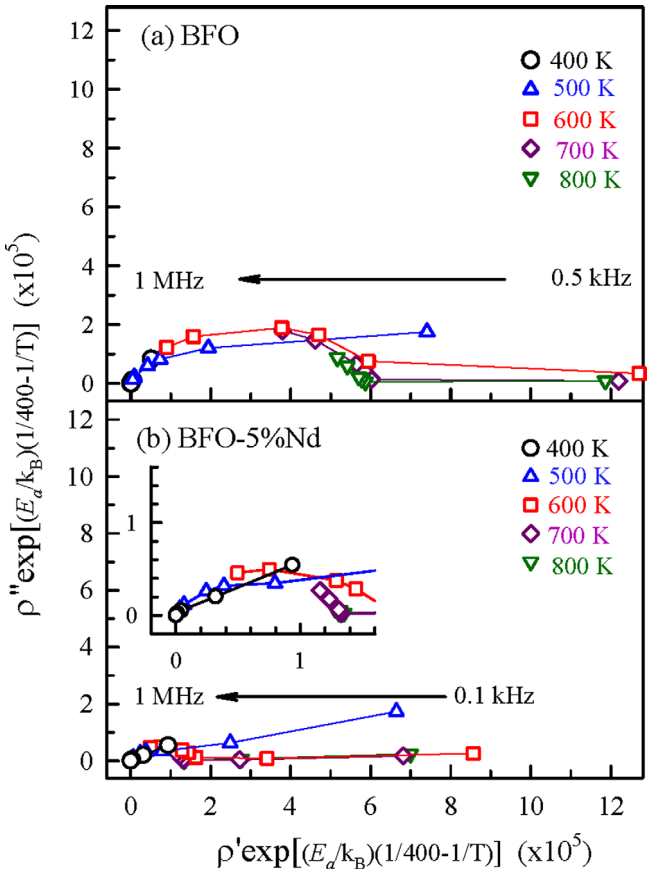

FIG. 6. (Color online) ρ'' exp$[(E_a/k_B)(1/400 - 1/T)]$ vs ρ' exp$[(E_a/k_B)(1/400 - 1/T)]$ at several temperatures. Frequencies are 0.1, 0.5, 10, 50, 100, 500, and 1000 kHz (from right to left). The activation energies, E_a, are 8710 and 8530 K for BFO and BFO-5%Nd, respectively.

CPEs for electrode impedance usually have steeper slopes than are shown in the right-hand parts of Fig. 6, however, a 3° slope was reported by Biswas *et al.*[16] for a 0.5M NH_4OH aqueous solution, which is comparable to the lowest slopes we observed.

The preceding qualitative attribution of the ρ'' versus ρ' arcs to grain boundaries or defects can be compared with our model predictions, where the higher barriers, $B + \Delta$, can be identified with the grain boundaries or defects. The sample preparation may have a large effect on permittivity in these materials. Dai and Akishige,[17] over their 20 to 130 °C range, obtained T and f dependencies of ε' and tan δ similar to ours for BFO annealed in vacuum. However, for BFO annealed in oxygen the behavior was much different, qualitatively similar to that observed by Kamba *et al.*[15] who reported T and f dependencies for T only up to 300 K.

IV. CONCLUSIONS

The across-barrier model can fairly well describe the low-frequency conductivities of BFO and BFO-5%Nd ceramics, which is responsible for the step-like dielectric relaxation in the region of 500–800 K. Compared with BFO, BFO-5%Nd has a lower intrinsic barrier, B, and a larger carrier concentration, n, indicating a higher conductivity. The deviations of conductivity from the barrier model below 650

K may be associated with the magnetoelectric coupling. The resistivity plots of scaled ρ'' versus ρ' implies a parallel combination of a resistor, R, and a CPE, in series with another CPE, which can usually be attributed to grain boundaries or to internal defects, and the series CPE can be attributed to electrode impedance.

ACKNOWLEDGMENTS

This work was supported by National Science Council of Taiwan Grant Nos. 97–2112-M-030-003-MY3 and NSC 100-2112-M-030-002-MY3.

[1]P. Fischer, M. Polomska, I. Sosnowska, and M. Szymański, J. Phys. C **13**, 1931 (1980).
[2]B. Ramachandran and M. S. Ramachandra Rao, Appl. Phys. Lett. **95**, 142505 (2009).
[3]F. Kubel and H. Schmid, Acta Crystallogr., Sect. B: Struct. Sci. **46**, 698 (1990).
[4]J. Li, J. Wang, M. Wuttig, R. Ramesh, N. Wang, B. Ruette, A. P. Pyatakov, A. K. Zvezdin, and D. Viehland, Appl. Phys. Lett. **84**, 5261 (2004).
[5]D. C. Arnold, K. S. Knight, F. D. Morrison, and P. Lightfoot, Phys. Rev. Lett. **102**, 027602 (2009).
[6]I. Levin, S. Karimi, V. Provenzano, C. L. Dennis, H. Wu, T. P. Comyn, T. J. Stevenson, R. I. Smith, and I. M. Reaney, Phys. Rev. B **81**, 020103(R) (2010).
[7]R. Palai, R. S. Katiyar, H. Schmid, P. Tissot, S. J. Clark, J. Robertson, S. A. T. Redfern, G. Catalan, and J. F. Scott, Phys. Rev. B **77**, 014110 (2008).
[8]S. T. Zhang, M. H. Lu, D. Wu, Y. F. Chen, and N. B. Ming, Appl. Phys. Lett. **87**, 262907 (2005).
[9]K. Singh, R. K. Kotnala, and M. Singh, Appl. Phys. Lett. **93**, 212902 (2008).
[10]S. Karimi, I. M. Reaney, I. Levin, and I. Sterianou, Appl. Phys. Lett. **94**, 112903 (2009).
[11]P. Pandit, S. Satapathy, P. K. Gupta, and V. G. Sathe, J. Appl. Phys. **106**, 114105 (2009).
[12]V. L. Mathe, K. K. Patankar, R. N. Patil, and C. D. Lokhande, J. Magn. Magn. Mater. **270**, 380 (2004).
[13]G. L. Yuan, S. W. Or, J. M. Liu, and Z. G. Liu, Appl. Phys. Lett. **89**, 052905 (2006).
[14]T.-H. Wang, C.-S. Tu, H.-Y. Chen, Y. Ding, T. C. Lin, Y.-D. Yao, V. H. Schmidt, and K.-T. Wu, J. Appl. Phys. **109**, 044101 (2011).
[15]S. Kamba, D. Nuzhnyy, M. Savinov, J. Sebek, J. Petzelt, J. Prokleska, R. Haumont, and J. Kreisel, Phys. Rev. B **75**, 024403 (2007).
[16]K. Biswas, L. Thomas, S. Chowdhury, B. Adhikari, and S. Sen, Int. J. Smart Sens.Intell. Syst. **1**, 922 (2008), see http://www.s2is.org/Issues/v1/n4/papers/paper6.pdf.
[17]Z. Dai and Y. Akishige, J. Phys. D: Appl. Phys. **43**, 445403 (2010).